ARMY RESEARCH LABORATORY

Navier-Stokes Computation of Shock Tube Exit Jet for Non-Ideal Blast Simulations

Bernard J. Guidos
Stephen J. Schraml
U.S. Army Research Laboratory

Dale K. Ota
Rockwell International Corporation
Science Center

ARL-TR-1105   APRIL 1996

Approved for public release; distribution is unlimited.

19960521 003

DTIC QUALITY INSPECTED 1

REPORT DOCUMENTATION PAGE

1. AGENCY USE ONLY (Leave blank)	2. REPORT DATE	3. REPORT TYPE AND DATES COVERED
	April 1996	Final

4. TITLE AND SUBTITLE

Navier-Stokes Computation of Shock Tube Exit Jet for Non-Ideal Blast Simulations

5. FUNDING NUMBERS

PR: 1L162618AH80

6. AUTHOR(S)

Guidos, B. J.; Schraml, S. J.; Ota*, D. K.

7. PERFORMING ORGANIZATION NAME(S) AND ADDRESS(ES)

U.S. Army Research Laboratory
Weapons Technology Directorate
Aberdeen Proving Ground, MD 21010-5066

8. PERFORMING ORGANIZATION REPORT NUMBER

9. SPONSORING/MONITORING AGENCY NAME(S) AND ADDRESS(ES)

U.S. Army Research Laboratory
Weapons Technology Directorate
Aberdeen Proving Ground, MD 21010-5066

10. SPONSORING/MONITORING AGENCY REPORT NUMBER

ARL-TR-1105

11. SUPPLEMENTARY NOTES

*Rockwell International Corporation Science Center, 1049 Camino Dos Rios, Thousand Oaks, CA 91360

12a. DISTRIBUTION/AVAILABILITY STATEMENT

Approved for public release; distribution is unlimited.

12b. DISTRIBUTION CODE

13. ABSTRACT (Maximum 200 words)

A computational fluid dynamics study of the exit jet of the U.S. Army Research Laboratory's 1.68-m diameter shock tube is presented. The shock tube exit jet provides a test environment in which to assess vehicle response to non-ideal blast. In the present study, time-accurate Navier-Stokes solutions are generated to simulate a shock tube exit jet test in which pressure probe measurements were obtained. The computational results are compared to the experimental data, as well as to analytical results and other empirical data. An examination is made of the jet flow field structure, and the computational accuracy and requirements are assessed.

14. SUBJECT TERMS

computational fluid dynamics	non-ideal blast	shock tube	unsteady flow
exit jet	nuclear weapons	shock waves	viscous flow

15. NUMBER OF PAGES

50

16. PRICE CODE

17. SECURITY CLASSIFICATION OF REPORT	18. SECURITY CLASSIFICATION OF THIS PAGE	19. SECURITY CLASSIFICATION OF ABSTRACT	20. LIMITATION OF ABSTRACT
Unclassified	Unclassified	Unclassified	

INTENTIONALLY LEFT BLANK

ACKNOWLEDGMENTS

INTENTIONALLY LEFT BLANK

TABLE OF CONTENTS

INTENTIONALLY LEFT BLANK

LIST OF FIGURES

INTENTIONALLY LEFT BLANK

1. INTRODUCTION

Non-ideal blast effects must be considered in the prediction of vehicle response and survivability to tactical nuclear weapon detonations. A non-ideal blast environment can be defined as one in which surface characteristics play a significant role. The environment of particular interest here is created by the presence of a thermal layer adjacent to the ground. The resulting non-ideal blast environment consists of an accelerated flow field that possesses a significantly elevated and sustained dynamic pressure following the initial blast wave. The Blast/Thermal Effects Branch of the Weapons Technology Directorate, U.S. Army Research Laboratory (ARL), is contributing to the development of capabilities to simulate and characterize ideal and non-ideal blast environments (Hisley, 1990; Schraml, 1991; Opalka, 1993; Loucks et al., 1995; Schraml, 1995; Ethridge et al., 1995). These computational and experimental capabilities will give the Army the necessary tools to accurately predict blast environments and to protect personnel and equipment.

As part of the ongoing non-ideal blast program, this report documents a computational fluid dynamics (CFD) study of the exit jet of ARL's 1.68-m diameter shock tube. The shock tube exit jet is being used to assess vehicle response to blast as well as to provide experimental validation for more complex CFD simulations. In the present CFD study, Navier-Stokes solutions are generated to simulate a shock tube exit jet test in which pressure probe measurements were obtained. The major objectives of the study are to (1) numerically simulate the exit jet flow field using a Navier-Stokes technique, (2) compare the computational results to analytical and experimental results, and (3) assess the computational accuracy and requirements.

2. SHOCK TUBE CONFIGURATION AND M113 APC TEST

The ARL 1.68-m diameter shock tube is located at the Spesutie Island shock tube facility at Aberdeen Proving Ground. The broad interest is the study of vehicle loading in the shock tube exit jet flow field. The shock tube exit jet can produce a high fidelity simulation of the dynamic flow associated with a thermally precursed nuclear weapon blast wave event. The jet diverges a small amount as a function of distance from the exit plane and develops a very high flow velocity.

Currently, the cross-sectional projected area is too small to adequately test full-scale military equipment; an attachable jet spreader is being developed to address this limitation (Loucks et al., 1996). Then the simulated non-ideal blast can uniformly engulf large military equipment such as wheeled and tracked vehicles. In the interim, both experiment and numerical calculation will provide background information necessary to produce high fidelity simulations of non-ideal blast using the shock tube exit jet.

The experimental data used in this report were gathered during a test conducted by the Blast/Thermal Effects Branch using the M113 armored personnel carrier (APC). Figure 1 is a frame of the video record of the test event showing the experimental setup. The M113 APC was parked perpendicular to the shock tube axis, with the upstream side located approximately 15.4 m from the shock tube exit plane. The approximate height and length of the M113 APC are 1.8 m and 4.9 m, respectively. A pitot probe was mounted on a steel frame and situated 10.64 m from the shock tube exit, 0.194 m below the projected shock tube axis. An in-tube pressure gauge (not shown in the figure) was located flush with the wall in the expansion section, 29.11 m upstream from the exit plane.

The total shock tube length is approximately 186 m, with the driver section length approximately 107 m. The wall thickness at the shock tube exit is approximately 11 mm. At the exit plane, the distance between the ground and the bottom of the shock tube is approximately 1.2 m. At the out-of-tube probe location, the distance between the ground and the projected bottom of the shock tube is approximately 1 m. The initial driver overpressure for this particular firing is 634.3 kPa (6.26 atm). The initial temperature in both the driver and expansion sections is ambient.
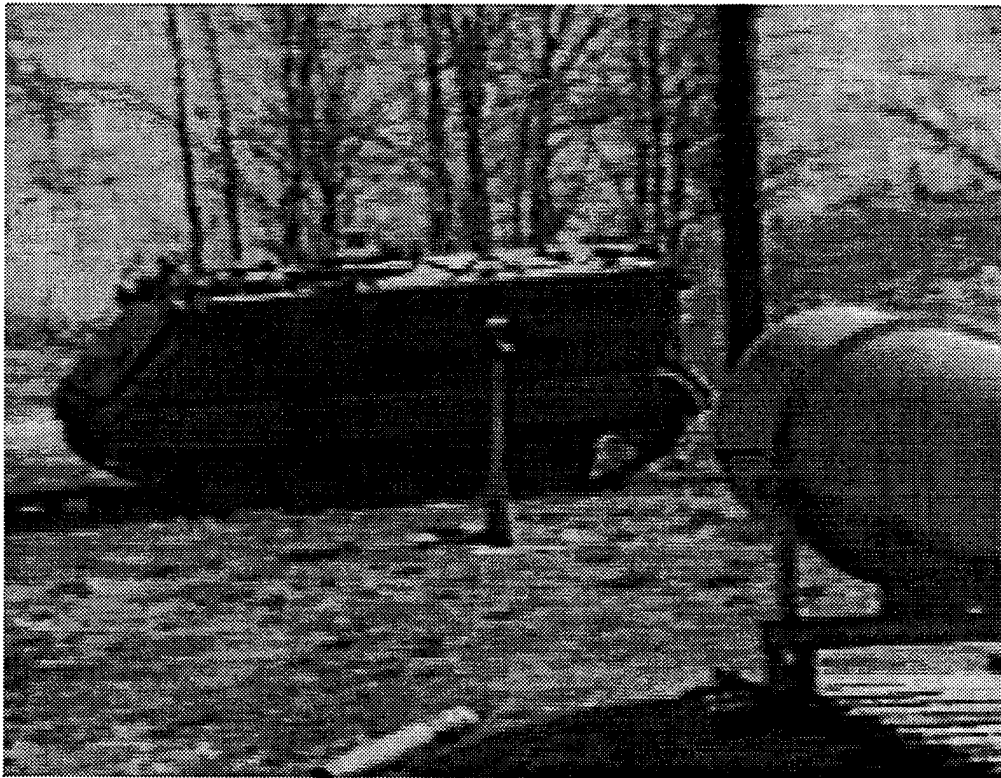
Figure 1. <u>Video Frame of 1.68-m Shock Tube Exit Jet Experimental Setup.</u>

3. COMPUTATIONAL MODEL

The numerical computations do not include the M113 APC, greatly simplifying the numerical grid construction and problem setup. The inclusion of the M113 APC (or other target vehicles), along with its dynamic response coupled to the CFD model, is a future task.

In the present study, the shock tube flow field is modeled using the unified solution algorithm for real gas in two dimensions (USA-RG2) CFD code, developed at the Rockwell International Science Center (RISC), Thousand Oaks, CA. The USA-RG2 code is used here to solve the axisymmetrical form of the Reynolds-averaged Navier-Stokes equations cast in generalized coordinates and strong conservation law form.

The equations are written in a finite volume formulation, and an implicit, approximately factored solution algorithm is used. The explicit convective terms are constructed using an upwind, total variation diminishing scheme which employs Roe's Riemann solver (Roe, 1981). The nonlinear form of the equations is solved by applying a Newton-iterative technique (Rai & Chakravarthy, 1986), although all solutions generated in this study used one iteration per time step. The viscosity terms are retained in each of the two coordinate directions, and a two-equation k-ϵ turbulence model for separated flows (Goldberg & Ota 1990) is used. Perfect gas behavior is assumed. Details of all the numerical aspects are presented or can be traced in reports by Chakravarthy (1986, 1988) and Chakravarthy et al. (1985, 1989).

The multi-zone grid capability of the USA-RG2 code was used for the computations reported here. Figure 2 illustrates the five computational grid zones used to model the flow field in and around the shock tube. Zone 1 is the driver section; Zone 2 is the expansion section; Zone 3 is an external region that abuts against the axis and exit plane; Zone 4 is the far wake region adjacent to the axis; Zone 5 is the region that surrounds the shock tube itself and extends upstream from the exit plane. All zonal boundaries are aligned, that is, zonal boundary points along two adjacent zonal boundaries share the same spatial coordinates.
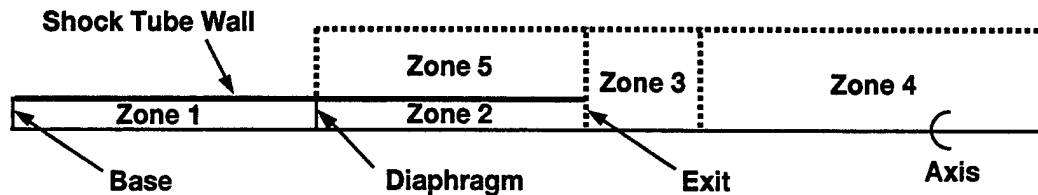
Note: Drawing not to scale

Figure 2. Computational Grid Zones for 1.68-m Shock Tube.

Figure 3 shows a magnified view of the grid at the shock tube exit. Radial grid point clustering is prescribed above and below the radial location corresponding to the shock tube wall in order to improve the resolution of the wall boundary layer and the free shear layer. Axial grid point clustering is prescribed at the exit plane to resolve the curvature of the shock as it exits the tube as well as the formation of the ring vortex. Additional axial grid point clustering (not shown in the figure) is prescribed at the shock tube base and diaphragm. Figure 3 also shows that the grid zones are defined so that the shock tube wall is modeled as a smooth, zero thickness wall. The numerous in-tube protuberances such as section joint weldings, the internally mounted test table (previously used for testing smaller equipment), and cavities (for cameras and other measurement devices) are ignored.

CFD solutions were generated using two different grids. They differ primarily by their respective number of grid points and spatial resolutions, as shown in Table 1. The initial grid was designed with relatively poor grid resolution. The refined grid was constructed after the initial grid solution was found to compare poorly with the out-of-tube probe data. Though the refined grid contains better resolution than the initial grid in some areas of the flow field domain judged to be critical, it also has less resolution in other areas judged to be less critical.

The downstream outflow boundary of Zone 4 is located approximately 290 m from the shock tube exit plane. The outer boundaries of Zones 3, 4, and 5 are positioned approximately 16 m from the axis. The upstream boundary of Zone 5 is positioned at the
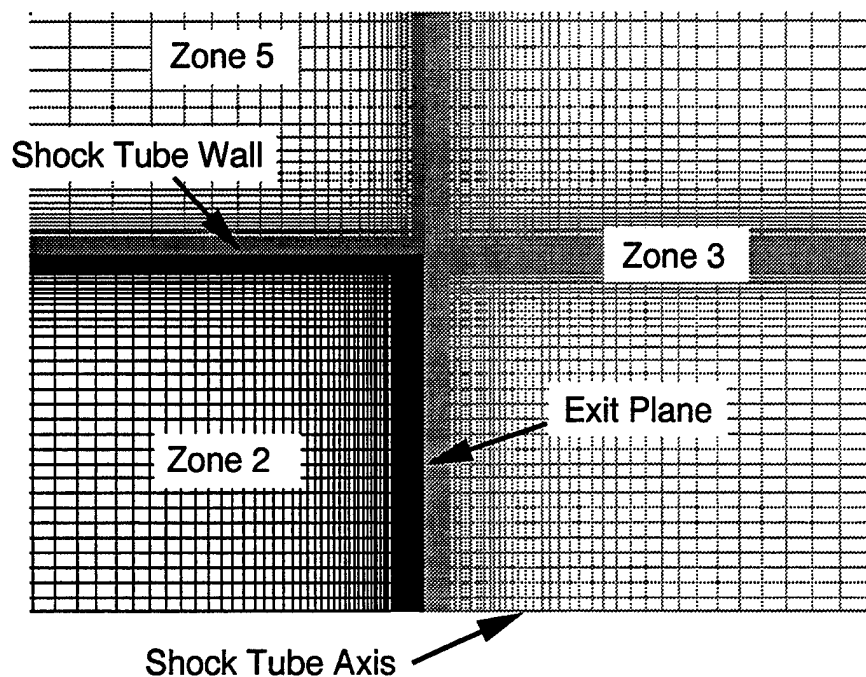
Figure 3. Magnified View of Computational Grid at Shock Tube Exit.

Table 1. Some Defining Parameters for Initial and Refined Grids.

	Initial Grid	Refined Grid
No. of Grid Points (axial × radial)		
Zone 1	201×31	140×65
Zone 2	299×31	280×65
Zone 3	101×100	130×150
Zone 4	31×100	80×150
Zone 5	21×70	80×86
Total number of grid points	30,170	65,680
Axial Spacing (m)		
At Base	0.01	0.1
At Diaphragm	0.01	0.01
At Exit	0.01	0.001
At Out-of-Tube Probe	0.45	0.24
Radial Spacing (m)		
At Axis	0.001	0.034
At Wall	0.001	0.0001

same axial location as the diaphragm. The boundary between Zones 3 and 4 is positioned approximately 25 m from the exit plane for the initial grid and 14 m from the exit plane for the refined grid.

The magnitude of the grid point clustering factor, F_l, was kept within ±10% for the refined grid, but was as high as 30% for the initial grid. The clustering factor is defined here as

$$F_l = \frac{\Delta s_{l+1} - \Delta s_l}{\Delta s_l} \times 100\% \qquad (1)$$

in which Δs_l and Δs_{l+1} are adjacent grid point spacings between grid indices l and $l+1$ in either of the two computational coordinate directions.

All grid elements except those in Zone 1 are initialized to ambient conditions. The ambient temperature, density, and pressure are assumed to be 288.15 K, 1.225 kg/m^3, and 101.325 kPa, respectively. The grid elements in Zone 1 are initialized to the driver conditions discussed in the previous section. The diaphragm rupture event is simply modeled as two separately initialized domains in contact with each other. All wall boundaries are modeled as adiabatic. The Zone 4 downstream outflow boundary, the Zone 5 upstream boundary, and the outer boundaries of Zones 3, 4, and 5 all use a zero normal gradient extrapolation boundary condition.

Two CFD solutions were generated using the initial grid. They differed only in the time steps that were prescribed as the solutions progressed. In each case, the time step was determined by prescribing a minimum allowable CFL (Courant-Friedrichs-Lewy) number. For the first solution, the CFL number was prescribed to be 1.0 at the onset of the computation and was increased to 20.0 by the time the shock exited the tube. For the second solution, the CFL number was prescribed to be 0.1 at the onset, increased to 20.0 before shock exit, decreased to 1.0 during shock exit, and increased up to 20.0 thereafter. This second solution was generated because the first solution compared poorly with the out-of-tube pressure probe data. However, the second solution showed no noticeable improvement in the pressure probe comparison. The initial grid results, to be shown in the next section, are those of the second, reduced CFL number, solution.

One CFD solution was generated using the refined grid. For the refined grid solution, the CFL number was prescribed to be 1.0 at the onset of the computation; increased to 20.0 before shock exit; decreased to 0.1 during shock exit; and increased to 20.0 thereafter. The relatively small CFL number of 0.1 used at shock exit was necessary to prevent the numerical solution from computing unreal flow conditions (specifically, negative densities), which led to termination of the computation.

The computations were performed on a Cray Y-MP computer at U.S. Army Corps of Engineers Waterways Experimental Station, Vicksburg, Mississippi, using a single processor. The initial grid solutions used approximately 100 central processing unit (CPU) hours and 2.3 million words of memory each, while the refined grid solution used approximately 200 CPU hours and 3.6 million words of memory. The numerical simulations were made to simulate the first 1600 ms of the event following diaphragm rupture.

4. RESULTS

4.1 Comparison with Analytical Results and Probe Data

Validation of the numerical results begins with an examination of the in-tube flow field before shock exit. A 1-D Riemann solution was generated to compare with the in-tube Navier-Stokes solutions. The Riemann solution, which excludes viscous effects, is an analytical solution valid along the entire length of the shock tube before shock exit. A representative comparison between the Navier-Stokes and Riemann solutions is included here for a time corresponding to 153.6 ms after diaphragm rupture. The in-tube flow field at this time is illustrated in Figure 4. From this view, the shock travels to the right and is within 1 meter from the exit. The contact surface trails the shock and separates the expanded driver air from the air that has been processed by the shock. The expansion waves move to the left.

6

Expansion Waves   **Contact Surface**   **Shock**

Base   **Diaphragm Location**   **Exit**

Note: Drawing not to scale
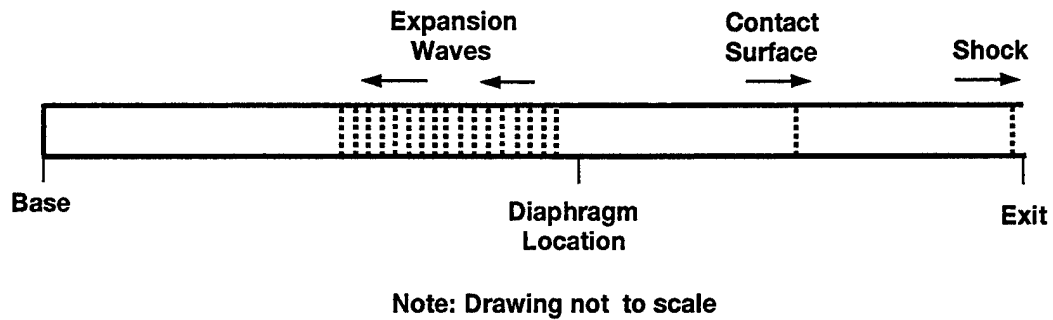
Figure 4. Approximate In-Tube Flow Field at 153.6 ms After Diaphragm Rupture.

Figures 5 through 8 show the density, pressure, velocity, and temperature from the Riemann solution compared to their respective axis values from the Navier-Stokes solutions at 153.6 ms. In all cases, the flow field properties and structural features compare well between the analytical and numerical solutions. The initial and refined grid Navier-Stokes solutions are plotted as a single curve because they were virtually indistinguishable in these comparisons. The Riemann comparisons serve as standard, preliminary indicators of grid resolution adequacy and solution integrity for the computed axial in-tube flow field before shock exit using both the initial and refined grids.
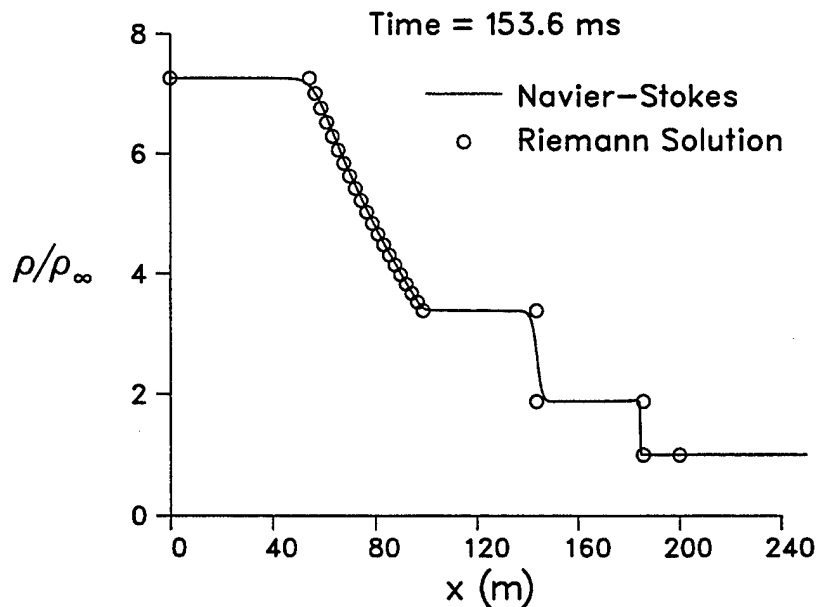
Figure 5. Computed Axis Density Compared to Riemann Solution, t=153.6 ms.
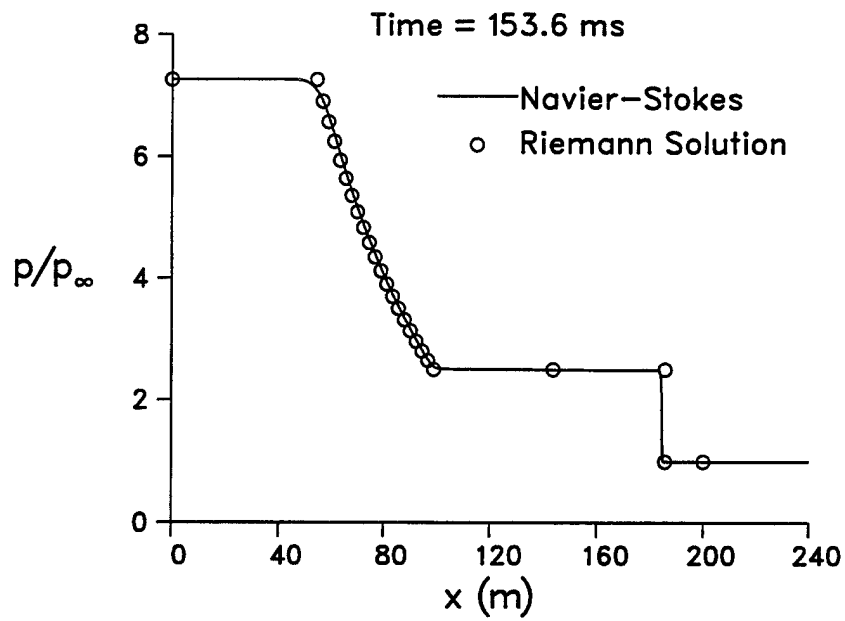
Figure 6. Computed Axis Pressure Compared to Riemann Solution, t=153.6 ms.
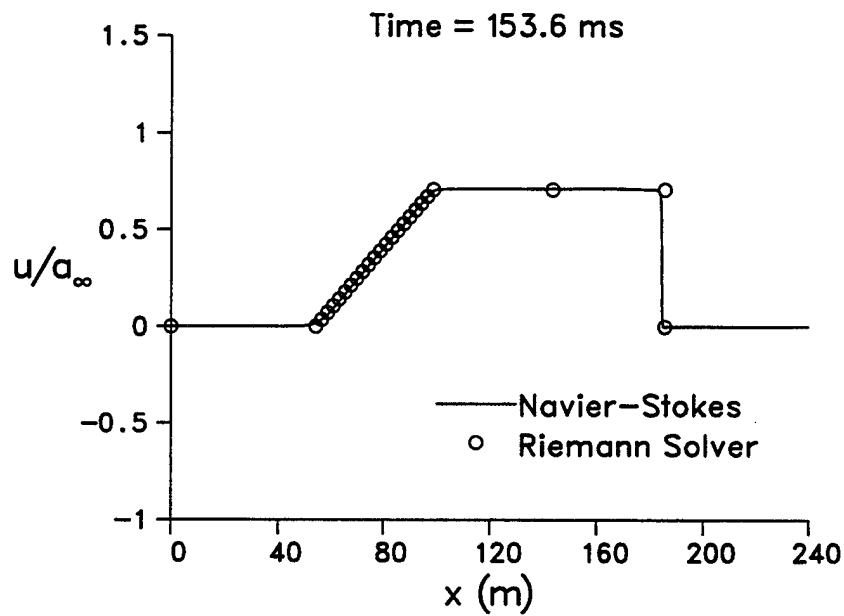
Figure 7. Computed Axis Velocity Compared to Riemann Solution, t=153.6 ms.
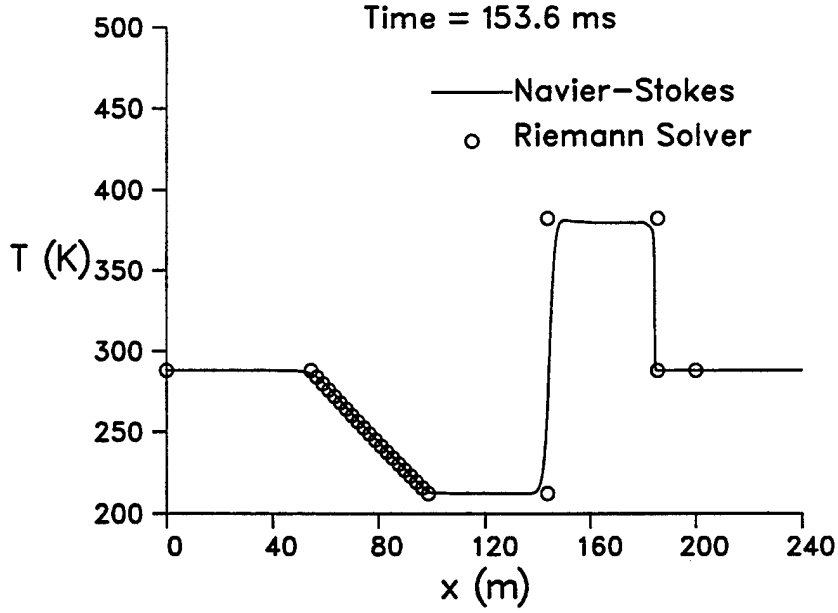
Figure 8. Computed Axis Temperature Compared to Riemann Solution, t=153.6 ms.

An examination of the computed shock tube wall boundary layer development before shock exit reveals additional insight into the accuracy of the Navier-Stokes solutions. As expected, the initial grid, with its relatively poor radial grid resolution near the wall, fails to capture the boundary layer throughout the duration of the computation. Specifically, no boundary layer velocity deficit can be discerned farther than one or two grid points from the wall. In this respect, the refined grid provides a substantial improvement in boundary layer resolution, although it does not completely resolve the laminar sublayer.

The boundary layer thickness from the refined grid solution can be compared to an analytical result. The boundary layer edge is assumed to be located where the axial velocity is 99% of the free stream (or, in this case, the axis) value. The boundary layer thickness δ is the distance from the wall to the boundary layer edge. An analytical expression for δ near a planar shock perpendicular to a flat plate is given by Sedney & Kitchens (1976) as

$$\delta = x_s Re_s^{-1/5} \qquad (2)$$

in which

$$Re_s = \frac{\gamma M_s^2 p_\infty x_s}{u_s \mu_\infty} \qquad (3)$$

In this expression, x_s is the distance from the shock; M_s is the shock Mach number; u_s is the shock speed; and p_∞ and μ_∞ are the free stream pressure and viscosity, respectively.

Figure 9 shows the comparison of wall boundary layer thickness for the refined grid solution and the 2-D analytical result. The analytical expression, Equation (2), applies only to the region between the contact surface and the shock. The comparison is shown at the same time as the previous Riemann comparisons (153.6 ms), just before shock exit. The maximum computed boundary layer thickness occurs at the contact surface. The analytical solution shows approximately one-third greater boundary layer thickness than the numerical solution. The comparison is considered favorable as a qualitative indicator of solution accuracy, considering the large sensitivity of boundary layer thickness.
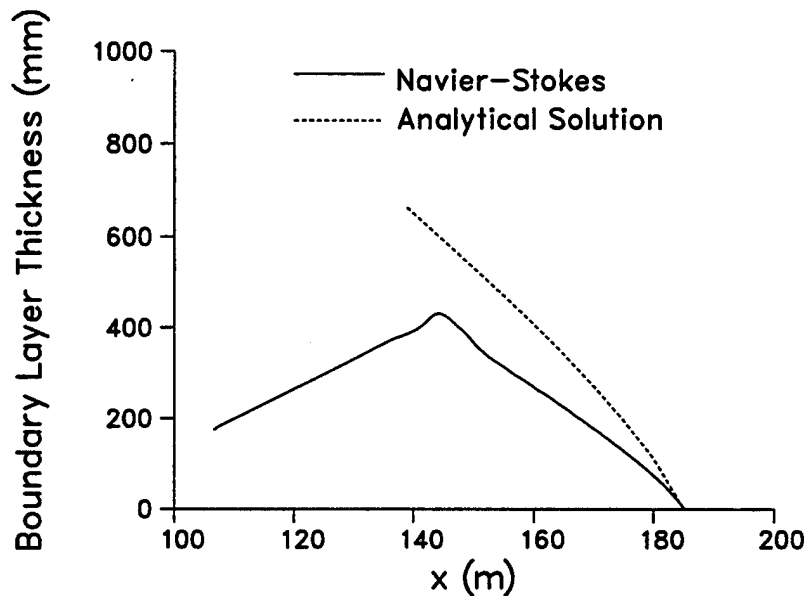
Figure 9. Computed and Analytical Boundary Layer Thicknesses, t=153.6 ms.

Figures 10 and 11 show the comparison of computed and measured pressures for the in-tube and out-of-tube probes. Whereas the computed pressure histories are referenced to the time of diaphragm rupture, the original measured pressure histories were referenced to the time at which the measurement equipment began recording. To compare the computed and measured results, the times of the measured data have been shifted so that the initial disturbances are aligned with those of the computed solutions.

Figure 10 shows the comparison of computed static overpressure $(p - p_\infty)$ with that of the in-tube probe. Within 650 ms after diaphragm rupture, the computed overpressures from both the initial and refined grid solutions differ from the measured overpressure by at most 10%. Beyond 650 ms, both computed pressure histories decrease more rapidly than the measured history. Near 400 ms, the refined grid solution shows noticeable improvement
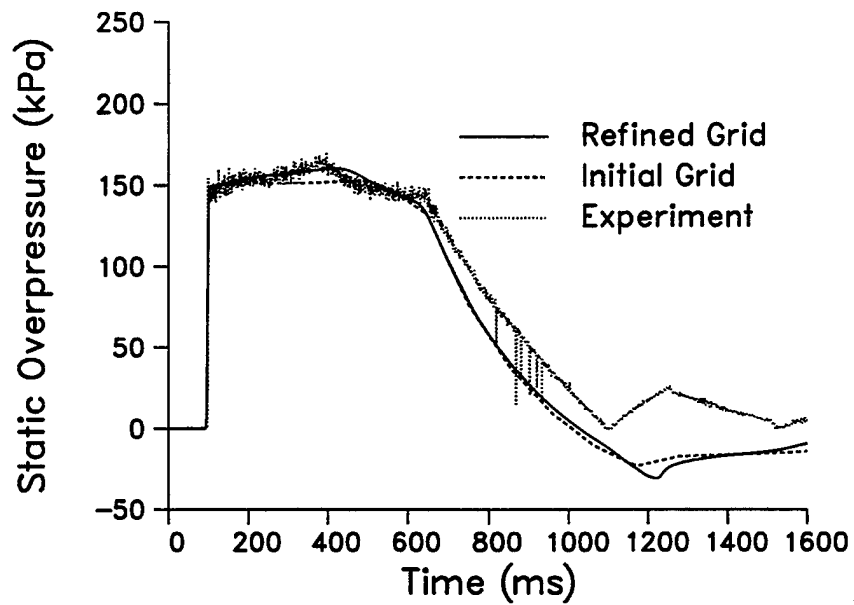
Figure 10. Computed and Measured In-Tube Gauge Static Overpressure.
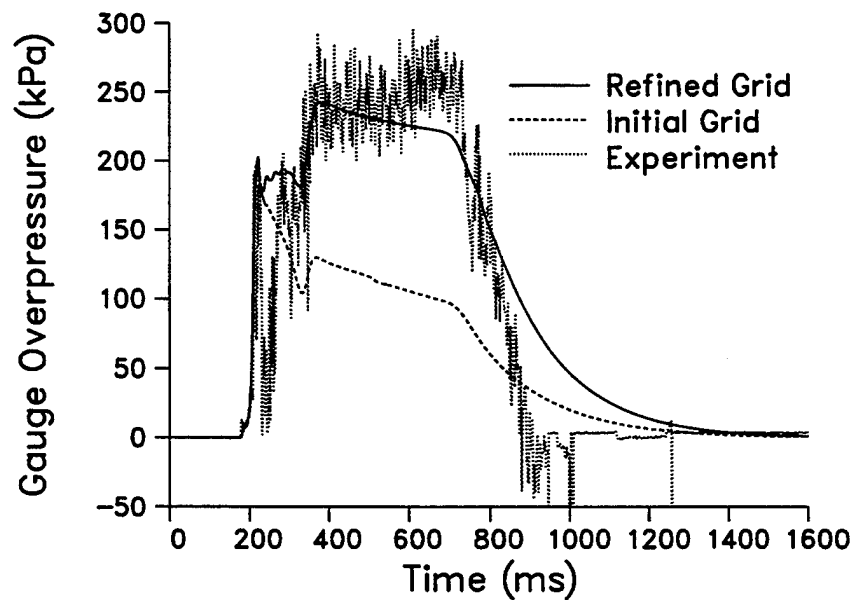
Figure 11. Computed and Measured Out-of-Tube Gauge Overpressure.

11

over the initial grid solution, capturing the pressure peak in the experimental data. It is inconclusive if the pressure peak is attributable to the presence of the boundary layer, which, as already mentioned, is not resolved by the initial grid. The computed displacement thickness of the in-tube boundary layer was examined and found to be two orders of magnitude less than the computed edge thickness already shown in Figure 9. A quasi-one-dimensional consideration, given the subsonic flow condition within the tube, states that a decrease in effective cross-sectional area will cause an increase in velocity and a decrease in pressure, exactly the opposite effect shown by the data. Instead, the pressure peak may be attributable to the elevated temperature levels within the boundary layer, which cause an increase in pressure, i.e., a thermodynamic effect. The pressure peak may also be an exit plane effect that propagates upstream and is more adequately captured by the improved axial resolution of the refined grid.

Figure 11 shows the comparison of the computed gauge overpressure $(p_p - p_\infty)$ with that of the out-of-tube probe. For $M \leq 1$, the pitot pressure (p_p) is the same as the stagnation pressure; for $M \geq 1$, it is the equivalent stagnation pressure behind a normal shock. The pressure measurements from the out-of-tube probe have fluctuations with amplitudes of approximately ± 30 kPa, much greater than the in-tube probe. The larger fluctuations associated with the out-of-tube probe are likely attributable to vibrations within the steel frame mount. The initial 10-kPa peak occurring at about 190 ms signifies the arrival of the weakened shock and is accurately captured in both computed solutions. The next 100 ms signify a highly transient period in which the measured overpressure abruptly rises to nearly 200 kPa, drops to less than 50 kPa, and recovers to approximately 150 kPa. Both computations capture the initial rise, but neither captures the abrupt drop and recovery. The refined grid solution overpressure, however, at least remains at a level comparable to the measurement at 300 ms.

The computational result does not capture the highly transient pressure probe response between 200 and 300 ms. The experimental results of Loucks et al. (1996) for a scaled model of the 1.68-m shock tube exit jet indicate that ground effects are negligible for several lower pressure cases with no vehicle. (No scaled tests were reported for the higher driver pressure examined here.) It may be argued that the presence of the M113 APC in the actual test may influence the out-of-tube probe measurement. The initial shock, traveling approximately 513 m/s, travels from the probe to the M113 in only 14 ms. The reflected shock travels upstream and interacts with the flow field, reaching the probe at approximately the same time as the first pressure rise to 200 kPa and contributing to the large pressure variations measured during this time period. In this scenerio, ground effects could also influence the pressure at the out-of-tube probe. A conclusive determination of the vehicle effect on the measured pitot pressure could be obtained by including a simple axisymmetrical body in the present axisymmetrical flow model and observing the computed pitot pressure response at the probe location.

The largest measured gauge overpressures occur between 400 and 700 ms, at which time, the driver gas reaches the probe. Large differences are apparent between the two computed solutions, with the initial grid solution predicting the gauge overpressure to only within about 50% of the measured values during this time interval. The refined grid solution, on the other hand, predicts the gauge overpressure within the fluctuations of the measured values from 400 to 600 ms.

Figure 11 also shows that the small additional rise in the measured out-of-tube gauge overpressure between 600 and 700 ms is not captured in the refined grid solution. The possibility that the M113 APC is influencing the pressure field at the probe location can be eliminated; Figure 12 shows the computed Mach number at the probe location for the refined grid solution. From 400 to 700 ms, the computed Mach number is approximately 1.44 (i.e., supersonic); therefore, a bow shock can be expected to form upstream from the vehicle. An ideal upper bound estimate of the shock standoff distance ahead of the vehicle can be obtained from the graph shown by Liepmann and Roshko (1957). The actual geometry is more complex than the cases available in the reference. However, assuming the limiting case of a flat nosed axisymmetrical geometry of diameter equal to the length of the M113 APC, the location of the bow shock vertex at Mach 1.44 is found to be approximately 1.5 m downstream from the probe. It is concluded that, during this time period, the pressure measurement is not likely to be influenced by the presence of the vehicle.
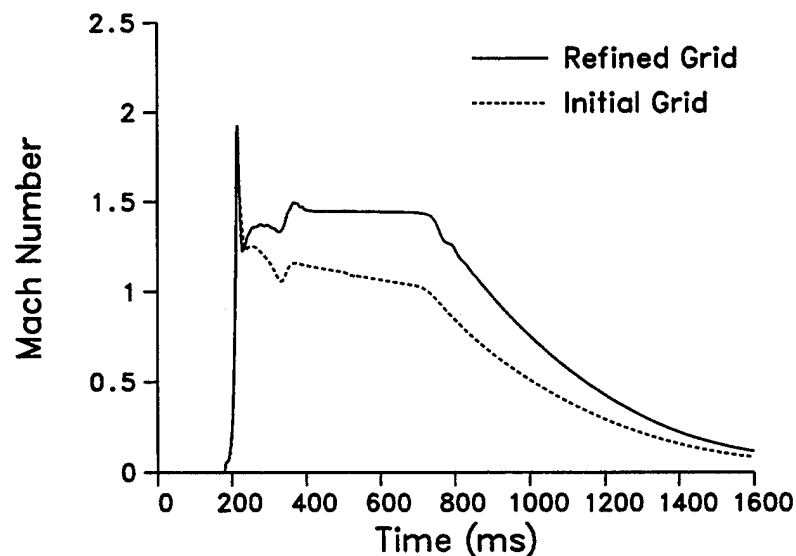
Figure 12. Computed Mach Number at Out-of-Tube Gauge Location.

Figure 11 also shows that, beyond 700 ms, the computed pressures decay more slowly than the measured values. The video record of the test shows the steel frame mount to be thrown at least 20 m by the force of the exit jet. The cloud of condensation (and possibly dust) in the video makes it impossible to visually estimate the time at which the steel frame becomes displaced. The poor agreement beyond 700 ms and the negative measured overpressures are possible indicators that the steel mounting frame has been displaced and the measured pressure is no longer valid.

Figure 13 shows the computed dynamic pressure of the initial and refined grid solutions. The dynamic pressure is the most relevant parameter for evaluating the response of bodies to drag forces that cause displacement and/or overturning. The figure shows that the refined grid solution predicts a significantly higher dynamic pressure at the out-of-tube probe location compared to the initial grid solution. The computed dynamic pressure of the refined grid solution reaches sustained magnitudes of 125 to 150 kPa, demonstrating the capacity of the 1.68-m shock tube exit jet to achieve conditions useful for simulating a particular non-ideal nuclear blast environment.
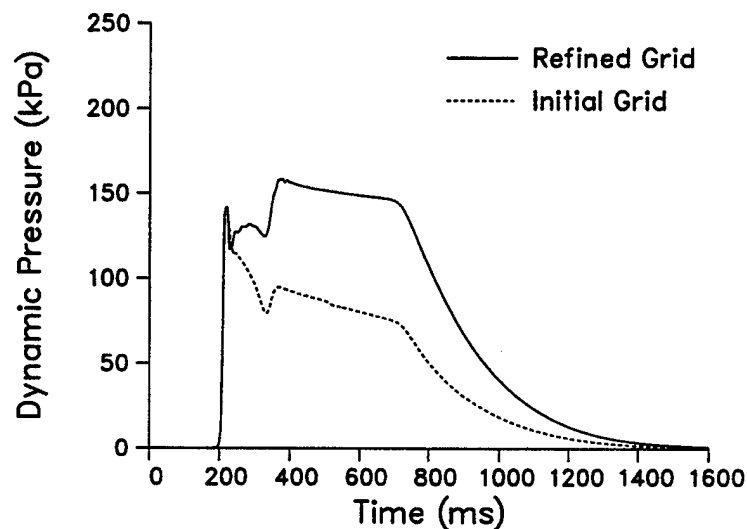
Figure 13. Computed Dynamic Pressure at Out-of-Tube Gauge Location.

4.2   Additional Examination of the Computed Jet Structure

The previous discussion demonstrated that the refined grid solution provides a significantly improved flow field prediction compared to the initial grid solution. Visualization of the two flow fields revealed additional differences between the initial and refined grid solutions which, for brevity, are not included here. The discussion made in this section of the computed exit jet flow field structure focuses on the refined grid solution.

Figure 14 shows a frame of the video record of the M113 test at a time when the shock just exited the tube and a ring vortex is the only visible flow structure. The vortex ring is visible in the photograph because the air (specifically, the water vapor) within it has reached temperatures low enough to condense. The low temperatures result from high velocity and low pressure within the vortex core. It is noted that only two frames of the video record show any visible sign of condensation within the ring vortex. The camera speed is 30 frames per second, equivalent to an interval of approximately 33.3 ms between images. It follows that the vortex is visibly condensed for a time duration of between 33.3 and 99.9 ms. It may be assumed that the vortex exists for a longer period of time than is apparent in the video but it is not visible.

Figure 14. Video Frame of Exit Jet Showing Ring Vortex.

Schlieren photographs (Love et al., 1959) and spark shadowgraphs (Schmidt & Lyon, 1988) of underexpanded sonic jets show the air, upon tube exit, to first expand and then recompress through a conical, oblique shock whose vertex is oriented upstream. Depending on the precise exit conditions, the shock vertex may be pointed or it may be capped with a normal shock (also referred to as a Mach disc or Riemann wave). The pattern formed by this initial expansion and recompression is the first in a periodic chain that forms as the jet develops. Such a chain is shown in Figure 15, a reproduced Schlieren photograph from Love et al. (1959), showing an exit jet from a 3.46-mm diameter nozzle having almost identical exit conditions (specifically M_j=1.0 and p_j/p_∞=1.76) as the present study. The chain-like structure, which consists of conically shaped features that appear triangular-like from this side view, decays and loses axisymmetry farther from the exit.

Figure 15. Reproduction of Schlieren Photograph of Jet taken from Love et al. (1959).

Figure 16 shows computed Mach contours from the refined grid solution at 157, 159, 161, and 172 ms after diaphragm exit. The shock exits the tube approximately 155 ms after diaphragm rupture. After exiting the tube, the shock curves around the wall, and by 159 ms, the curvature has propagated to the axis. By 161 ms, the initial expansion emanating from the wall has reached the axis; that is, the air on the axis has begun to expand. The exit flow conditions become nearly sonic. By 172 ms, the initial expansion is fully formed and its downstream edge intersects the axis approximately 3/4 diameter from the exit. The air begins the process of forming a shock that is smeared as it is captured in the computed solution.

Figure 17 shows computed vorticity magnitude contours from the refined grid solution for times of 157, 159, 161, and 172 ms after diaphragm rupture. Of primary interest is the ring vortex, which is computed to reach its largest magnitude immediately upon tube exit. The numerical solution shows the vortex to rapidly move away from the exit and dissipate, separating from the region of vorticity that constitutes the shear layer of the jet. Although not shown in the figure, the numerical solution shows the computed vortex to dissipate
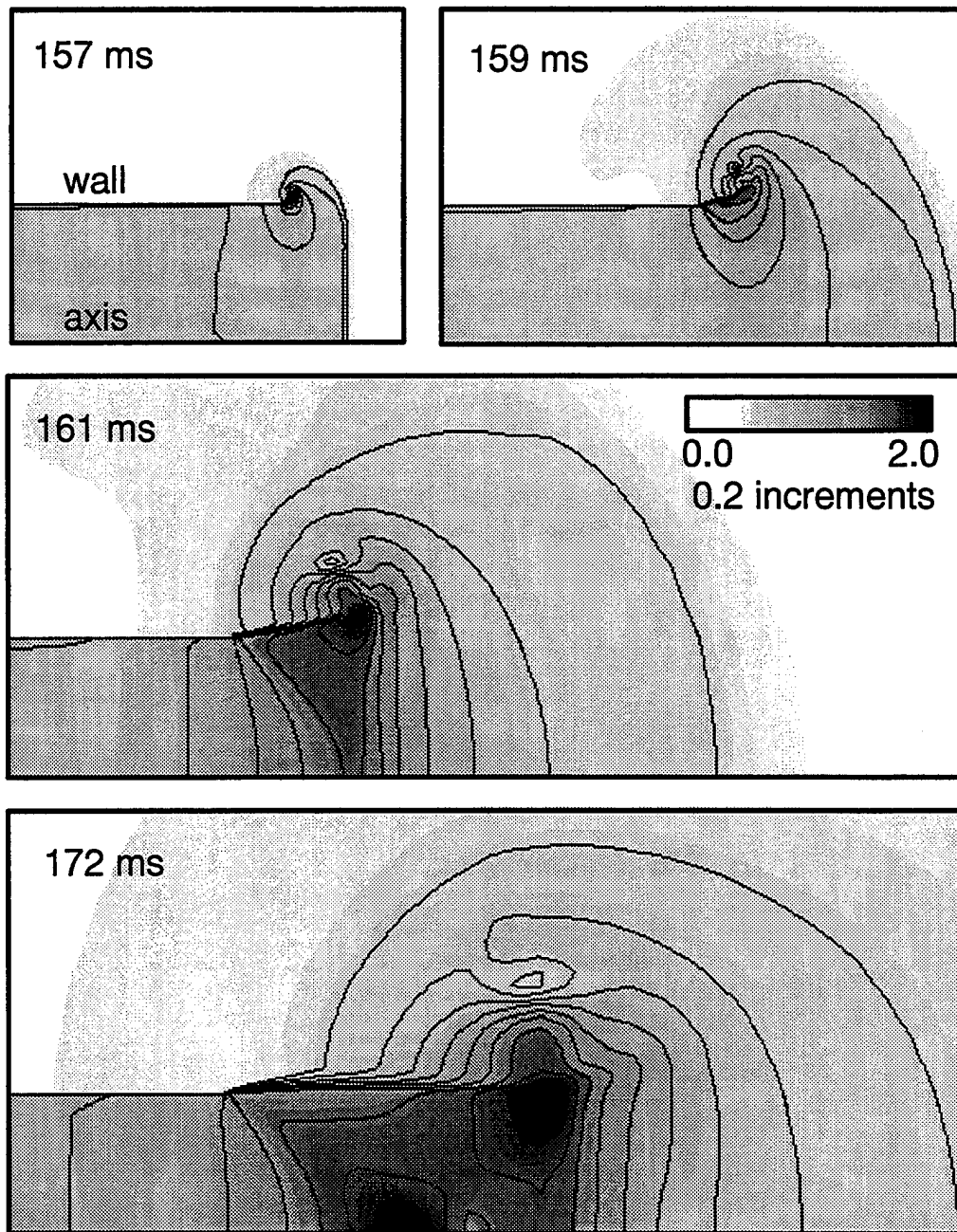
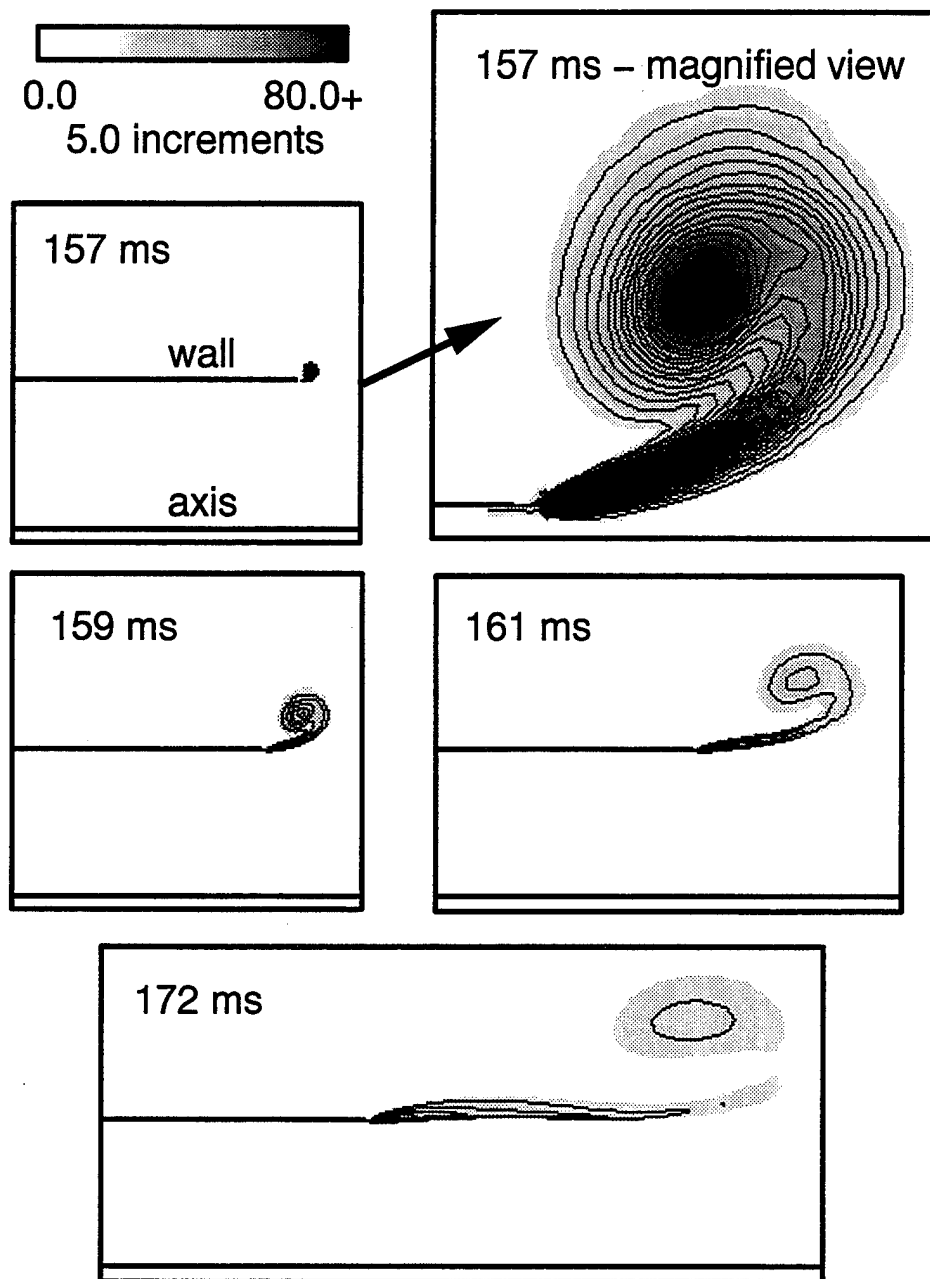Figure 16. Computed Mach Contours as Shock Exits Tube.

Figure 17. Computed Vorticity Magnitude Contours (ω) as Shock Exits Tube.

almost completely by approximately 75 ms after shock exit, which is qualitatively consistent with the video record. The separate contributions of inviscid and viscous effects were not studied here, but an inviscid computation of the problem using the same grid would quantify the importance of the two effects on the vortex formation and history, as well as on other aspects of the flow field.

Figures 18 through 21 show flow field contours at 648 ms after diaphragm rupture, highlighting the chain-like structure as it is captured within the numerical solution. Figure 18 illustrates that the accuracy of the computed wavelength and spatial decay of the chain-like structure can significantly affect the pitot pressure at the probe location. In contrast, the dynamic pressure contours in Figure 19 show less amplitude variation along the axis near the probe location, demonstrating that the sensitivity of the predicted dynamic pressure (and vehicle response) to the computed wavelength and spatial decay of the chain-like structure are probably minimal.

Figures 20 and 21 show Mach number and static pressure contours, respectively, at 648 ms after diaphragm rupture. At this time, the computed jet is well developed and more steady, compared to other times during the event. A chain-like structure is apparent in both sets of contours. Direct examination of the computed solution data represented by Figures 20 and 21 shows the exit Mach number on the axis to be M_j=1.08 and the exit pressure to be p_j/p_∞=1.79. The computed flow structure can be qualitatively compared to the Schlieren photograph of Figure 15. The conical shape of the flow structures is not readily apparent in the contour plots of the computed solution, indicating a possible need for improved grid resolution to more precisely resolve the embedded flow gradients.

The computed primary wavelength of the chain-like structure can be obtained directly from the solution data represented in Figures 18, 20, or 21. The primary wavelength normalized by the tube diameter is denoted w/d, and the computed value is assumed here to be the distance along the axis from the tube exit to the first maximum pressure location. The computed flow field solution shows this distance to be 1.48 diameters. This value can be compared to the semi-empirical correlation of the primary wavelength given by Love et al. (1959) as

$$w/d = 1.55\sqrt{M_j^2(p_j/p_\infty) - 1} - 0.55\sqrt{M_j^2 - 1} \tag{4}$$

Using the computed exit values given above, Equation (4) yields a value of w/d=1.40, approximately 6% less than the value in the computed flow field solution.

The graphical correlations of Love et al. (1959) also indicate that, for the exit conditions of the present study, the initial expansion outside the shock tube will focus very close to the axis. At this location, the expansion will culminate as either the vertex of an oblique, conical shock or, at most, a Mach disc of very small diameter.

19
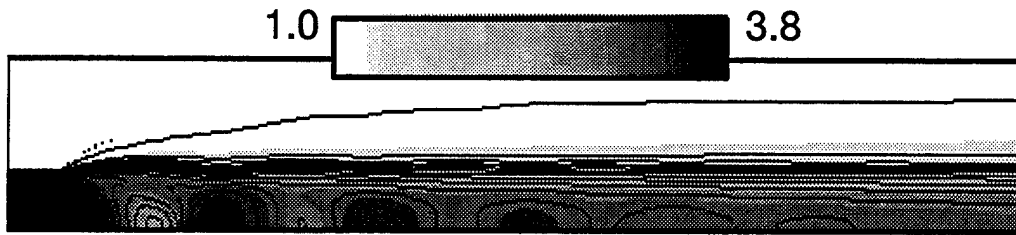
Figure 18. Computed Pitot Pressure Contours (p_p/p_∞) in 0.2 Increments, t=648 ms.

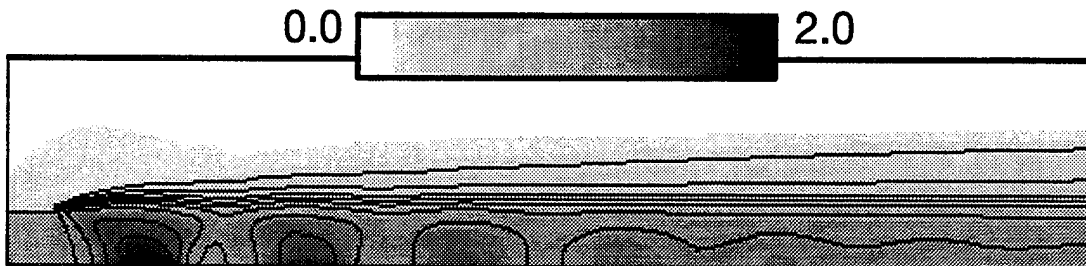Figure 19. Computed Dynamic Pressure Contours (q) in 0.1 Increments, t=648 ms.

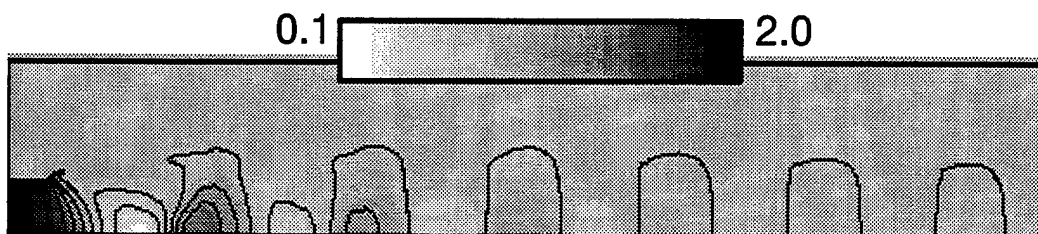Figure 20. Computed Mach Contours in 0.2 Increments, t=648 ms.

Figure 21. Computed Pressure Contours (p/p_∞) in 0.2 Increments, t=648 ms.

An evaluation can be made of the accuracy of the computed focal length, which is the distance along the axis from the exit plane to the shock vertex or to the Riemann wave. The graphical correlations of focal length given by Love et al. (1959) do not include the exit conditions of the present case. However, using the available condition M_j=1.0 and the computed condition p_j/p_∞=1.79, the focal length is graphically shown to be about 0.85 diameter. If, in the computed solution, the focal length is measured from the exit to the downstream location on the axis where the first pressure minimum occurs, the computed focal length is 0.88 diameter, about 3.5% greater than the graphically obtained value.

Finally, Figure 22 shows a video frame of the exit jet impinging and engulfing the M113 APC. The front edge of the M113 is just barely visible, and this video frame represents the final frame in which the vehicle can be seen. Most of the jet is visibly condensed and suggests that the implementation of a jet spreader would allow the vehicle to be completely immersed in the jet.

Figure 22. Video Frame of Exit Jet Engulfing M113 Armored Personnel Carrier.

5. CONCLUSION

A CFD study of an exit jet from the ARL 1.68-m diameter shock tube has been presented. The time-dependent Navier-Stokes code USA-RG2, developed at Rockwell International Science Center, was used in axisymmetrical mode to compute the shock tube flow field from the time of diaphragm rupture through the duration of the event (about 1600 ms).

Three CFD solutions were generated, employing two different grids. All three CFD solutions compared well with a Riemann solution for times preceding shock exit. Only the refined grid solution resolved the wall boundary layer enough to compare reasonably well with an analytical solution for boundary layer thickness between the shock and contact surface before shock exit. All three solutions compared reasonably well with the measured in-tube probe pressure history, although the refined grid solution more clearly captured a peak in the data thought to be attributable to boundary layer effects. Only the refined grid solution compared reasonably well with the measured out-of-tube probe pressure history. The dynamic pressure response outside the shock tube, the most relevant parameter for evaluating dynamic vehicle response, was significantly different between the initial and refined grid solutions.

The experimental data were available from a shock tube test conducted on the M113 APC, which was parked downstream from the shock tube exit plane, beyond the out-of-tube pressure probe. This particular firing corresponded to a shock tube case having an initial driver overpressure (p/p_∞) of 6.26, the largest of three shots. The computational model did not include the M113 APC, and some differences in the computed and measured overpressures at the out-of-tube probe location were attributed to the presence of the vehicle influencing the measured pressure history.

Comparison of the computed jet flow structure to video records of the test and to empirical data showed mixed results. The computation captured the brief appearance of the ring vortex that follows initial shock exit, and the computed time duration of the vortex was consistent with the video record. The computation also captured the chain-like structure of expansions and recompressions within the jet, although their conical shapes were not captured precisely enough to reproduce the triangular appearance as illustrated by a Schlieren photograph of a jet with almost identical exit conditions. Comparison of the computed primary wavelength of the chain-like structure with an empirical correlation indicated agreement within 6%. Comparison of the computed focal length of the initial expansion (i.e., the location of the shock vertex or Mach disc) with an empirical, graphical correlation indicated agreement within 3.5%. Improved axial grid resolution in the region downstream from the exit could improve the resolution of the flow structure, although dynamic pressures near the out-of-tube probe location may not be substantially affected.

The refined grid computation was performed using approximately 200 hours of single processor CPU time on a Cray Y-MP computer. Substantial reduction in the required CPU time for this class of problem can be achieved by using parallel processing capabilities that

are becoming available on various computing platforms. Reductions may also be achieved as a result of determining the importance of modeling issues such as viscosity, turbulence, or boundary layer effects, which substantially affect the CPU usage. Additional time savings could have been achieved in the present study by using the USA code capability that allows inactive zones to be carried along without numerical processing – an example of the importance of user expertise as it pertains to computational efficiency.

Overall, the study demonstrates that the CFD model can accurately simulate important aspects of the dynamic flow associated with the shock tube exit jet. The study provides a benchmark of the computational requirements for the problem. The details should contribute to the formulation of CFD simulations that model target vehicle response to non-ideal blast environments.

INTENTIONALLY LEFT BLANK

6. REFERENCES

Chakravarthy, S.R., "The Versatility and Reliability of Euler Solvers Based on High-Accuracy TVD Formulations," AIAA Paper No. 86-0243, 1986.

Chakravarthy, S.R., "High Resolution Upwind Formulations for the Navier-Stokes Equations," von Karman Institute for Fluid Dynamics, Lecture Series 1988-05, Computational Fluid Dynamics, March 7-11, 1988.

Chakravarthy, S.R., K.Y. Szema, U.C. Goldberg, and J.J. Gorski, "Application of a New Class of High Accuracy TVD Schemes to the Navier-Stokes Equations," AIAA Paper No. 85-0165, 1985.

Chakravarthy, S.R., K.Y. Szema, and J.W. Haney, "Unified Nose-to-Tail Computational Method for Hypersonic Vehicle Applications," AIAA Paper No. 89-2564, 1989.

Ethridge, N.H., J.H. Keefer, J.E. Crepeau, R.G. Ekler, L.W. Kennedy, C.E. Needham, and S.H. Rogers, "Real Surface (Non-Ideal) Effects on Nuclear Explosion Airblast from PRISCILLA-Type Events, Part I: Comparison and Evaluation of Ideal and Non-Ideal Airblast From PRISCILLA Computations; and Part II: SHARC Hydrocode Calculations of the PRISCILLA Event (Phase I)," ARL-CR-277, U.S. Army Research Laboratory, Aberdeen Proving Ground, Maryland, October 1995.

Goldberg, U.C., and D.K. Ota, "A k-ϵ Near Wall Formulation for Separated Flows," AIAA Paper No. 90-1492, 1990.

Hisley, D.M., "Computational Studies for 1/57-Scale Large Blast Simulator (LBS) Configurations with the BLAST2D Code," BRL-TR-3152, U.S. Army Ballistic Research Laboratory, Aberdeen Proving Ground, Maryland, September 1990. (AD A227514)

Liepmann, H.W. and A. Roshko, Elements of Gas Dynamics, Wiley, New York, 1957.

Loucks, R.B., P.C. Muller, R.L. Thane, T.C. Cline, L.G. Ferguson, and C. Mermagen, "Simulation of Non-Ideal Blast with a Shock Tube Exit Jet," ARL-TR-984, U.S. Army Research Laboratory, Aberdeen Proving Ground, Maryland, February 1996.

Love, E.S., C.E. Grigsby, L.P. Lee, and M.J. Woodling, "Experimental and Theoretical Studies of Axisymmetric Free Jets," National Aeronautics and Space Administration Technical Report R-6, 1959.

Opalka, K.O., "Numerical Simulation of the Flow in a 1:57-Scale Axisymmetric Model of a Large Blast Simulator," ARL-TR-111, U.S. Army Research Laboratory, Aberdeen Proving Ground, Maryland, April 1993. (AD A265551)

Rai, M.M., and Chakravarthy, S., "An Implicit Form for the Osher Upwind Scheme," AIAA Journal, Vol. 24, No. 5, pp. 735-743, 1986.

Roe, P.L., "Approximate Riemann Solvers, Parameter Vectors, and Difference Schemes," Journal of Computational Physics, Vol. 43, pp. 357-372, 1981.

Schmidt, E.M., and D.H. Lyon, "Measurement of the Flow from the Open End of a Shock Tube," Proceedings of TTCP Panel W-2, KTA-7 Workshop on the Computation of Weapon Launch Blast Overpressure, BRL-SP-76, U.S. Army Ballistic Research Laboratory, Aberdeen Proving Ground, Maryland, December 1988. (AD B130619)

Schraml, S.J., "Performance Predictions for the Large Blast/Thermal Simulator Based on Experimental and Computational Results," BRL-TR-3232, U.S. Army Ballistic Research Laboratory, Aberdeen Proving Ground, Maryland, May 1991. (AD A235728)

Schraml, S.J., "Exploratory Analysis of Helium Layer Usage for Dynamic Pressure Enhancement in the Large Blast/Thermal Simulator," ARL-TR-869, U.S. Army Research Laboratory, Aberdeen Proving Ground, Maryland, September 1995. (AD A264396)

Sedney, R., and C.W. Kitchens, "Turbulent Boundary Layers in Blast Wave and Shock Tube Flows," BRL-R-1907, U.S. Army Ballistic Research Laboratories, Aberdeen Proving Ground, Maryland, August 1976. (AD A029435)

LIST OF SYMBOLS

a speed of sound

d shock tube diameter

k turbulent kinetic energy

M Mach number

M_s shock Mach number

p pressure

p_p pitot pressure

q dynamic pressure, normalized by ρV^2

T temperature

t time

u velocity component in x direction

u_s shock speed

V total velocity

w primary wavelength of periodic structure

x distance along shock tube axis, measured from base, positive toward tube exit

x_s axial distance from shock

Greek Symbols

ϵ turbulent dissipation rate

δ boundary layer thickness

γ ratio of specific heats, taken as 1.4

μ coefficient of viscosity

ρ density

ω vorticity magnitude, normalized by d/a_∞

Subscripts

j shock tube exit condition

∞ free stream condition

INTENTIONALLY LEFT BLANK

NO. OF
COPIES   ORGANIZATION

2   DEFENSE TECHNICAL INFO CTR
     ATTN DTIC DDA
     8725 JOHN J KINGMAN RD
     STE 0944
     FT BELVOIR VA 22060-6218

1   DIRECTOR
     US ARMY RESEARCH LAB
     ATTN AMSRL OP SD TA
     2800 POWDER MILL RD
     ADELPHI MD 20783-1145

1   DIRECTOR
     US ARMY RESEARCH LAB
     ATTN AMSRL OP SD TL
     2800 POWDER MILL RD
     ADELPHI MD 20783-1145

1   DIRECTOR
     US ARMY RESEARCH LAB
     ATTN AMSRL OP SD TP
     2800 POWDER MILL RD
     ADELPHI MD 20783-1145

ABERDEEN PROVING GROUND

5   DIR USARL
     ATTN AMSRL OP AP L (305)

13 COMMANDER
US ARMY ARMAMENT RD&E CTR
ATTN AMSTA AR AET A
M AMORUSO
E BROWN
S CHUNG
A FARINA
J GRAU
H HUDGINS
W KOENIG
C LIVECCHIA
G MALEJKO
C NG
J THOMASOVICH
W TOLEDO
B WONG
PICATINNY ARSENAL NJ 07806-5000

5 COMMANDER
US ARMY ARMAMENT RD&E CTR
ATTN AMSTA AR CCH B
E FENNELL
T LOUZEIRO
D KITCHEN
B KONRAD
F QUEVEDO
PICATINNY ARSENAL NJ 07806-5000

4 COMMANDER
US ARMY ARMAMENT RD&E CTR
ATTN AMSTA AR FSE
E ANDRICOPOULIS
K CHEUNG
A GRAF
D LADD
PICATINNY ARSENAL NJ 07806-5000

6 COMMANDER
US ARMY ARMAMENT RD&E CTR
ATTN AMSTA AR CCL B
D CONWAY
D DAVIS
K HAYES
M PINCAY
F PUZYCKI
W SCHUPP
PICATINNY ARSENAL NJ 07806-5000

1 COMMANDER
US ARMY ARMAMENT RD&E CTR
ATTN AMSTA AR CCH A
J DIFUCCI
PICATINNY ARSENAL NJ 07806-5000

1 COMMANDER
US ARMY MISSILE COMMAND
ATTN AMSMI RD SS AT
B WALKER
REDSTONE ARSENAL AL 35898-5010

3 U.S. ARMY RESEARCH OFFICE
ATTN G ANDERSON
K CLARK
T DOLIGOWSKI
PO BOX 12211
RESEARCH TRIANGLE PARK NC 27709-2211

2 DIRECTOR
US ARMY BENET LABORATORY
ATTN SMCAR CCB R
P AALTO
S SOPOK
WATERVALIET NY 12189

1 DIRECTOR
US BELVOIR RD&E CTR
ATTN SATBE FED
N BLACKWELL
FORT BELVOIR VA 22060-5606

2 COMMANDER
UNITED STATES MILITARY ACADEMY
DEPARTMENT OF CIVIL
AND MECHANICAL ENGINEERING
ATTN M COSTELLO
A DULL
WEST POINT NY 10996

6 DIRECTOR
NASA AMES RESEARCH CTR
ATTN MS 258-1
L SCHIFF
T HOLST
D CHAUSSEE
T EDWARDS
G MOLVIK
S LAWRENCE
MOFFETT FIELD CA 94035

1 DIRECTOR
NASA AMES RESEARCH CTR
ATTN MS 202-14 T HOLTZ
MOFFETT FIELD CA 94035

1 DIRECTOR
NASA AMES RESEARCH CTR
ATTN MS 202A-1 M RAI
MOFFETT FIELD CA 94035

NO. OF COPIES	ORGANIZATION	NO. OF COPIES	ORGANIZATION
3	DIRECTOR NASA LANGLEY RESEARCH CTR ATTN TECHNICAL LIBRARY J SOUTH F WILCOX LANGLEY STATION HAMPTON VA 23665	3	DIRECTOR SANDIA NATIONAL LABS ATTN MS-1511 D BARNETTE F BLOTTNER M WALKER PO BOX 5800 ALBUQUERQUE NM 87185-5800
3	COMMANDER AIR FORCE ARMAMENT LABORATORY ATTN AFATL/FXA G ABATE S ADELGREN B SIMPSON EGLIN AFB FL 32542-5434	5	DIRECTOR SANDIA NATIONAL LABS ATTN DOC CONTROL 3141 C GHANBARI DIV 6215 MS 1127 A CHABAI DIV 7112 D GARDNER DIV 1421 J MCGLAUN DIV 1541 PO BOX 5800 ALBUQUERQUE NM 87185-5800
2	COMMANDER US NAVAL SURFACE WARFARE CTR ATTN CODE R44 A WARDLAW F PRIOLO WHITE OAK LABORATORY SILVER SPRING MD 20903-5000	1	DIRECTOR LOS ALAMOS NATIONAL LABORATORY ATTN MS C930 B HOGAN LOS ALAMOS NM 87545
2	COMMANDER US NAVAL SURFACE WARFARE CTR ATTN F MOORE T HYMES DAHLGREN VA 22448	1	HQDA ATTN SARD TT F MILTON WASHINGTON DC 20310-0103
2	COMMANDER USAF WRIGHT AERONAUTICAL LABS ATTN AFWAL/FIMG J SHANG WPAFB OH 45433-6553	2	HQDA ATTN SARD TR K KOMINOS R CHAIT WASHINGTON DC 20310-0103
1	COMMANDER ARNOLD ENG & DEV CTR CALSPAN FIELD SERVICE ATTN MS 600 J BENEK AAFB TN 37389	2	DIRECTOR FEDERAL EMERGENCY MNGMNT AGENCY ATTN PUBLIC RELATIONS OFFICE TECHNICAL LIBRARY WASHINGTON DC 20472
2	DIRECTOR SANDIA NATIONAL LABS ATTN MS-1636 W OBERKAMPF W WOLFE PO BOX 5800 ALBUQUERQUE NM 87185-5800	1	CHAIRMAN DOD EXPLOSIVES SAFETY BOARD BLDG 1 ROOM 856 C HOFFMAN 2461 EISENHOWER AVENUE ALEXANDRIA VA 22331-0600
		1	DIRECTOR OF DEFENSE RES AND ENGINEERING ATTN DD TWP WASHINGTON DC 20301

NO. OF COPIES	ORGANIZATION
1	DIRECTOR DEFENSE INTELLIGENCY AGENCY ATTN DT 2 WPNS & SYS DIVISION WASHINGTON DC 20301
1	ASSISTANT SECRETARY OF DEFENSE ATOMIC ENERGY ATTN DOCUMENT CONTROL WASHINGTON DC 20301
9	DIRECTOR DEFENSE NUCLEAR AGENCY ATTN CSTI TECHNICAL LIBRARY DDIR DFSP NANS OPNA SPSD SPTD DFTD TDTR WASHINGTON DC 20305
1	CHAIRMAN JOINT CHIEFS OF STAFF ATTN J5 R&D DIVISION WASHINGTON DC 20301
3	COMMANDER FIELD COMMAND DNA ATTN FCPR FCTMOF NMHE KIRTLAND AFB NM 87115
1	U S ARMY RESEARCH DEVELOPMENT AND STANDARDIZATION GROUP UK ATTN R REICHENBACH PSC 802 BOX 15 FPO AE 09499-1500
10	CENTRAL INTELLIGENCE AGENCY DIR DB STANDARD ATTN GE 47 HQ WASHINGTON DC 20505
2	COMMANDER US ARMY NRDEC ATTN AMSNA D D SIELING STRNC UE J CALLIGEROS NATICK MA 01762

NO. OF COPIES	ORGANIZATION
1	DIRECTOR ADVANCED RESEARCH PROJECTS AGENCY ATTN TECHNICAL LIBRARY 3701 NORTH FAIRFAX DRIVE ARLINGTON VA 22203-1714
2	COMMANDER US ARMY NRDEC ATTN SSCNC YSD J ROACH SSCNC WST A MURPHY KANSAS STREET NATICK MA 10760-5018
2	COMMANDER US ARMY CECOM ATTN AMSEL RD AMSEL RO TPPO P FT MONMOUTH NJ 07703-5301
1	COMMANDER US ARMY NGIC ATTN RESEARCH & DATA BRANCH 220 7TH STREET NE CHARLOTTESVILLE VA 22901-5396
1	US ARMY MISSILE & SPACE INTELLIGENCE CENTER ATTN AIAMS YDL REDSTONE ARSENAL AL 35898-5500
1	COMMANDING OFFICER CODE L51 NAVAL CIVIL ENGINEERING LAB ATTN J TANCRETO PORT HUENEME CA 93043-5003
3	COMMANDER US ARMY CORPS OF ENGINEERS WATERWAYS EXPERIMENT STATION ATTN CEWES SS R J WATT CEWES SE R J INGRAM CEWES TL TECH LIBRARY PO BOX 631 VICKSBURG MS 39180-0631
2	COMMANDER US ARMY STRATEGIC DEFENSE COMMAND ATTN CSSD H MPL TECH LIB CSSD H X DAVIES PO BOX 1500 HUNTSVILLE AL 35807

NO. OF COPIES	ORGANIZATION
1	OLAC PL TSTL ATTN D SHIPLETT EDWARDS AFB CA 93523-5000
1	AFIT ENY ATTN LTC HASEN WRIGHT PATTERSON AFB OH 45433-6583
1	AFIT ATTN TECHNICAL LIBRARY BLDG 640 B WRIGHT PATTERSON AFB OH 45433
2	AIR FORCE ARMAMENT LABORATORY ATTN AFATL DOIL AFATL DLYV EGLIN AFB FL 32542-5000
1	DIRECTOR LAWRENCE LIVERMORE NATIONAL LAB ATTN TECH INFO DEPT L 3 PO BOX 808 LIVERMORE CA 94550
1	DIRECTOR NATIONAL AERONAUTICS & SPACE ADMIN ATTN SCIENTIFIC & TECH INFO FAC PO BOX 8757 BWI AIRPORT BALTIMORE MD 21240
1	FTD NIIS WRIGHT PATTERSON AFB OH 45433
1	DIRECTOR IDAHO NATIONAL ENGINEERING LAB ATTN SPEC PROGRAMS J PATTON 2151 NORTH BLVD MS 2802 IDAHO FALLS ID 83415
4	DIRECTOR IDAHO NATIONAL ENGINEERING LAB EG&G IDAHO INC ATTN R GUENZLER MS 3505 R HOLMAN MS 3510 R BERRY W REED PO BOX 1625 IDAHO FALLS ID 83415
3	INST FOR ADVANCED TECHNOLOGY UNIV OF TEXAS AT AUSTIN ATTN W REINECKE T KIEHNE D BARNETT 4030-2 W BRAKER LANE AUSTIN TX 78759-5329

NO. OF COPIES	ORGANIZATION
2	UNIV OF CALIFORNIA DAVIS DPT OF MECHANICAL ENGINEERING ATTN H DWYER B MEAKIN DAVIS CA 95616
1	UNIVERSITY OF MARYLAND DPT OF AEROSPACE ENGINEERING ATTN J ANDERSON JR COLLEGE PARK MD 20742
1	UNIVERSITY OF TEXAS DPT OF AEROSPACE ENGINEERING AND ENGINEERING MECHANICS ATTN D DOLLING AUSTIN TEXAS 78712-1055
1	UNIVERSITY OF DELAWARE DPT OF MECHANICAL ENGINEERING ATTN L SCHWARTZ NEWARK DE 19716
4	UNIVERSITY OF CINCINNATI DPT OF AEROSPACE ENGINEERING ATTN K GHIA P KHOSLA S RUBIN G SLATER MAIL LOCATION 70 CINCINNATI OH 45221
1	UNIVERSITY OF FLORIDA DPT OF ENGINEERING SCIENCES ATTN C HSU GAINESVILLE FL 32611
2	UNIV OF ILLINOIS URBANA CHAMPAIGN DPT OF MECHANICAL AND INDUSTRIAL ENGINEERING ATTN A ADDY C DUTTON 114 MECHANICAL ENGINEERING BUILDING 1206 WEST GREEN ST. URBANA IL 61801
3	PENNSYLVANIA STATE UNIVERSITY DPT OF MECHANICAL ENGINEERING ATTN K KUO C MERKLE G SETTLES UNIVERSITY PARK PA 16802

NO. OF COPIES	ORGANIZATION	NO. OF COPIES	ORGANIZATION
1	FLORIDA ATLANTIC UNIVERSITY DPT OF MECHANICAL ENGINEERING ATTN W CHOW BOCA RATON FL 33431	2	FC DNA ATTN DASIAC BLDG 20676 1680 TEXAS ST SE KIRTLAND AFB NM 87117-5669
1	NORTH CAROLINA STATE UNIVERSITY DPT OF MECHANICAL AND AEROSPACE ENGINEERING ATTN D MCCRAE BOX 7910 RALEIGH NC 27695-7910	1	R&D ASSOCIATES ATTN G GANONG PO BOX 9377 ALBUQUERQUE NM 87119
1	UNIVERSITY OF MINNESOTA ARMY HIGH PERF COMP RES CTR ATTN T TEZDUYAR 1100 WASHINGTON AVE SOUTH MINNEAPOLIS MN 55415	3	ALLIANT TECHSYSTEMS INC ATTN M SWENSON S BECKER S BURRETTA MAIL STATION MN48-3700 7225 NORTHLAND DR BROOKLYN PARK MN 55428
1	MIT ATTN TECHNICAL LIBRARY CAMBRIDGE MA 02139	1	ALLIANT TECHSYSTEMS INC ATTN ROGER A RAUSCH 600 2ND STREET NE HOPKINS MN 55343-8367
1	STATE UNIVERSITY OF NEW YORK MECHANICAL & AEROSPACE ENGINEERING ATTN P GIVI BUFFALO NY 14260	1	CARPENTER RESEARCH CORP ATTN H CARPENTER 27520 HAWTHORNE BLVD SUITE 263 PO BOX 2490 ROLLING HILLS ESTATES CA 90274
2	UNIVERSITY OF MARYLAND INSTITUTE FOR ADV COMPUTER STUDIES ATTN L DAVIS G SOBIESKI COLLEGE PARK MD 20742	1	AEROSPACE CORPORATION ATTN TECH INFO SERVICES PO BOX 92957 LOS ANGELES CA 90009
1	NORTHROP UNIVERSITY ATTN F SAFFORD 5800 W ARBOR VITAE STREET LOS ANGELES CA 90045	1	THE BOEING COMPANY ATTN AEROSPACE LIBRARY PO BOX 3707 SEATTLE WA 98124
1	CALIFORNIA INSTITUTE OF TECHNOLOGY ATTN T AHRENS 1201 E CALIFORNIA BLVD PASADENA CA 91109	2	FMC CORPORATION ADVANCED SYSTEMS CENTER ATTN J DROTLEFF C KREBS MDP 95 BOX 58123 2890 DE LA CRUZ BLVD SANTA CLARA CA 95052
2	MDA ENGINEERING INC ATTN J STEINBRENNER D ANDERSON 500 E BORDER ST SUITE 401 ARLINGTON TX 76010	1	SVERDRUP TECHNOLOGY INC SVERDRUP CORPORATION AEDC ATTN B HEIKKINEN MS 900 ARNOLD AFB TN 37389-9998
2	PHYSICS INTERNATIONAL CORP PO BOX 5010 SAN LEANDRO CA 94577-0599		

NO. OF COPIES	ORGANIZATION
1	KTECH CORPORATION ATTN E GAFFNEY 901 PENNSYLVANIA AVE NE ALBUQUERQUE NM 87111
1	EATON CORPORATION DEFENSE VALVE & ACTUATOR DIV ATTN J WADA 2338 ALASKA AVE EL SEGUNDO CA 90245-4896
2	MCDONNELL DOUGLAS ASTRONAUTICS CORP ATTN R HALPRIN KA HEINLY 5301 BOLSA AVENUE HUNTINGTON BEACH CA 92647
4	KAMAN AVIDYNE ATTN R RUETENIK 2 CP S CRISCIONE R MILLIGAN 83 SECOND AVENUE NORTHWEST INDUSTRIAL PARK BURLINGTON MA 01830
1	GENERAL RESEARCH CORP ATTN H KING PO BOX 6770 SANTA BARBARA CA 93160-6770
7	KAMAN SCIENCES CORP ATTN PA ELLIS J FORKOIS T HAYDEN W LEONARD R PROZAN F SHELTON E STATTON 1500 GARDEN OF THE GODS RD. COLORADO SPRINGS CO 80907
4	HERCULES INC ALLEGANY BALLISTICS LABORATORY ATTN J CONDON W NYGA J PARRILL J VILES PO BOX 210 ROCKET CTR WV 26726

NO. OF COPIES	ORGANIZATION
1	FORD MOTOR COMPANY ATTN T GIELDA 15031 S COMMERCE DR SUITE 100 DEARBORN MI 48120
2	VRA INC. ATTN C LEWIS B BHUTTA PO BOX 50 BLACKSBURG VA 24060
1	BLACK & VEATCH ENGINEERS ARCHITECTS ATTN H LAVERENTZ 1500 MEADOW LAKE PARKWAY KANSAS CITY MO 64114
2	APPLIED RESEARCH ASSOCIATES INC ATTN J KEEFER N ETHRIDGE PO BOX 548 ABERDEEN MD 21001
1	ADA TECHNOLOGIES INC ATTN J BUTZ HONEYWELL CENTER SUITE 110 304 INVERNESS WAY SOUTH ENGLEWOOD CO 80112
1	MEDICOMP TECHNOLOGIES INC. ATTN S CHAKRAVARTHY 5540 WEMBLY AVE. AGOURA CA 91301
2	SCIENCE CENTER ROCKWELL INTERNATIONAL CORP ATTN S RAMAKRISHNAN D OTA 1049 CAMINO DOS RIOS THOUSAND OAKS CA 91360
1	ORLANDO TECHNOLOGY INC ATTN D MATUSKA 60 SECOND STREET BLDG 5 SHALIMAR FL 32579
2	THE RALPH M PARSONS COMPANY ATTN T JACKSON LB TS PROJECT MANAGER 100 WEST WALNUT STREET PASADENA CA 91124

NO. OF COPIES	ORGANIZATION
1	SAIC ATTN J GUEST 2301 YALE BLVD SE SUITE E ALBUQUERQUE NM 87106
1	SAIC ATTN N SINHA 501 OFFICE CENTER DR APT 420 FT WASHINGTON PA 19034-3211
1	SUNBURST RECOVERY INC ATTN C YOUNG PO BOX 2129 STEAMBOAT SPRINGS CO 80477
1	SVERDRUP TECHNOLOGY INC ATTN R STARR PO BOX 884 TULLAHOMA TN 37388
3	S CUBED A DIVISION OF MAXWELL LABS INC ATTN TECHNICAL LIBRARY R DUFF K PYATT PO BOX 1620 LA JOLLA CA 92037-1620
2	S CUBED A DIVISION OF MAXWELL LABS INC ATTN C NEEDHAM L KENNEDY 2501 YALE BLVD SE ALBUQUERQUE NM 87106
3	SRI INTERNATIONAL ATTN GR ABRAHAMSON J GRAN DR B HOLMES 333 RAVENWOOD AVENUE MENLO PARK CA 94025
1	TRW BALLISTIC MISSILE DIVISION ATTN H KORMAN MAIL STATION 526 614 PO BOX 1310 SAN BERNADINO CA 92402
1	BATTELLE TWSTIAC 505 KING AVENUE COLUMBUS OH 43201-2693

NO. OF COPIES	ORGANIZATION
1	THERMAL SCIENCE INC ATTN R FELDMAN 2200 CASSENS DRIVE ST LOUIS MO 63026
2	DENVER RESEARCH INSTITUTE ATTN J WISOTSKI TECHNICAL LIBRARY PO BOX 10758 DENVER CO 80210
3	SOUTHWEST RESEARCH INSTITUTE ATTN DR C ANDERSON S MULLIN A B WENZEL PO DRAWER 28255 SAN ANTONIO TX 78228-0255

ABERDEEN PROVING GROUND

1	CDR USATECOM ATTN AMSTE TE F L TELETSKI
1	CDR USATHAMA ATTN AMSTH TE
1	CDR USATC ATTN STEC LI
5	COMMANDER US ARMY ARMAMENT RD&E CTR ATTN AMSTA AR FSF T R LIESKE J MATTS F MIRABELLE R PUHALLA J WHITESIDE
64	DIRECTOR US ARMY RESEARCH LABORATORY ATTN AMSRL SC C NIETUBICZ AMSRL SC CC R ANGELINI P COLLINS C ELLIS J GROSH D HISLEY R SHEROKE AMSRL SC I W STUREK AMSRL SC S R PEARSON AMSRL SL CM E FIORVANTE AMSRL WT N J INGRAM AMSRL WT NA R KEHS

NO. OF COPIES	ORGANIZATION

AMSRL WT NC
  R LOTTERO
  R LOUCKS
  A MIHALCIN
  P MULLER
  S SCHRAML
AMSRL WT ND J MILETTA
AMSRL WT NF L JASPER
AMSRL WT NG T OLDHAM
AMSRL WT NH J CORRIGAN
AMSRL WT P
  A HORST
  E SCHMIDT
AMSRL WT PA
  P CONROY
  G KELLER
  D KRUCZYNSKI
  T MINOR
  M NUSCA
AMSRL WT PB
  M BUNDY
  G COOPER
  H EDGE
  K FANSLER
  E FERRY
  J GARNER
  B GUIDOS
  K HEAVEY
  D LYON
  A MIKHAIL
  V OSKAY
  P PLOSTINS
  J SAHU
  K SOENCKSEN
  P WEINACHT
AMSRL WT PC
  G ADAMS
  R FIFER
AMSRL WT PD
  B BURNS
  W DRYSDALE
  G GAZONAS
  D HOPKINS
  R LIEB
  S WILKERSON
AMSRL WT TA W GILLICH
AMSRL WT TB W DEROSSET
AMSRL WT TC A DIETRICH
AMSRL WT TD R FREY
AMSRL WT W
  C MURPHY

AMSRL WT WB
  F BRANDON
  T BROWN
  L BURKE
  W D'AMICO
  B DAVIS
  D HEPNER
  M HOLLIS
AMSRL WT WC
  R VON WAHLDE
AMSRL WT WD
  T KOTTKE
  C STUMPFEL